Physics of the Earth and Planetary Interiors 276 (2018) 93–105

Contents lists available at ScienceDirect

Physics of the Earth and Planetary Interiors

journal homepage: www.elsevier.com/locate/pepi

A time-averaged regional model of the Hermean magnetic field

E. Thébault [a,*], B. Langlais [a], J.S. Oliveira [b], H. Amit [a], L. Leclercq [c]

[a] LPG UMR-CNRS 6112 "Laboratoire de Planétologie et Géodynamique de Nantes", University of Nantes, 2, rue de la Houssinière BP 92208, 44322 NANTES Cedex 3, France
[b] Institut de Physique du Globe de Paris, Sorbonne Paris Cité, Univ. Paris Diderot, CNRS, 1 rue Jussieu F-75005, Paris, France
[c] University of Virginia, Charlottesville, VA 22903, USA

ARTICLE INFO

Article history:
Received 31 January 2017
Received in revised form 26 June 2017
Accepted 13 July 2017
Available online 20 September 2017

ABSTRACT

This paper presents the first regional model of the magnetic field of Mercury developed with mathematical continuous functions. The model has a horizontal spatial resolution of about 830 km at the surface of the planet, and it is derived without any a priori information about the geometry of the internal and external fields or regularization. It relies on an extensive dataset of the MESSENGER's measurements selected over its entire orbital lifetime between 2011 and 2015. A first order separation between the internal and the external fields over the Northern hemisphere is achieved under the assumption that the magnetic field measurements are acquired in a source free region within the magnetospheric cavity. When downward continued to the core-mantle boundary, the model confirms some of the general structures observed in previous studies such as the dominance of zonal field, the location of the North magnetic pole, and the global absence of significant small scale structures. The transformation of the regional model into a global spherical harmonic one provides an estimate for the axial quadrupole to axial dipole ratio of about $g_2^0/g_1^0 = 0.27$. This is much lower than previous estimates of about 0.40. We note that it is possible to obtain a similar ratio provided that more weight is put on the location of the magnetic equator and less elsewhere.

1. Introduction

The Mariner 10 mission flybys (Ness et al., 1974, 1975) showed that Mercury's magnetic environment is distinctive from other planets. It is characterized by a comparatively weaker internal field and by a stronger external field due to its shorter distance to the Sun. The first magnetic field measurements suggested that the Hermean internal field is mostly dipolar and may be stronger in the northern than in the southern hemisphere. This feature can be well represented by a single equivalent magnetic dipole with a northward offset along Mercury's spin axis [e.g., Ng and Beard, 1979]. Despite this very intriguing feature one had to wait until the launch of the MESSENGER spacecraft in 2004 to further investigate the Hermean magnetic field.

The MESSENGER (MErcury Surface, Space ENvironment, GEochemistry and Ranging) spacecraft operated around Mercury from March 2011 until April 2015. It confirmed that the internal field is mostly symmetric with respect to the planet's spin axis (Anderson et al., 2008; Anderson et al., 2011). The field is longitudinally essentially symmetric and can be represented by an equivalent dipole field shifted northward of about 0.196 R_M with respect to the center of the planet (Anderson et al., 2012; Johnson et al., 2012), with R_M = 2440 km the radius of Mercury. When expressed in terms of Spherical Harmonics (SH) coefficients in the planetocentric reference frame, this dipole offset implies that the ratio between the axial quadrupole and dipole SH terms is about 0.4.

The dipole representation is a mathematical convenience useful to approximate large scale planetary magnetic fields with a minimum number of parameters. It should be kept in mind that we should not attribute a physical meaning to this offset (Lowes, 1994). On Earth 98% of the geomagnetic field on the surface at epoch 2015 can be explained by a single dipole shifted away from the center by about 578 km or 0.091 Earth's radius (Laundal and Richmond, 2016). In the case of Mercury this offset representation has had strong implications on our understanding of the origin of the Hermean internal field, because the global magnetic feature it describes is difficult to reproduce by numerical dynamo simulations [e.g., Wicht et al., 2007; Cao et al. et al., 2014; Wicht and Heyner, 2014]. In the following study we propose a different representation of the time-average Hermean magnetic field through a regional modeling of MESSENGER's measurements over its entire lifetime.

The reassessment of the dipole offset hypothesis is justified for several reasons. First, this hypothesis does not take into account the deformation of the Hermean field by the solar wind as measured by the MESSENGER mission. The solar wind interacts

* Corresponding author.
E-mail address: erwan.thebault@univ-nantes.fr (E. Thébault).

http://dx.doi.org/10.1016/j.pepi.2017.07.001
0031-9201/

with the Mercury's main magnetic field which causes the field lines in the magnetosphere to be compressed in the day side and elongated toward local midnight. Second, the elliptical orbital configuration of MESSENGER does not allow probing the internal magnetic field of Mercury over its southern hemisphere. This lack of measurements represents a real challenge for planetary scale magnetic field representations. This, in turn, has possible consequences on the estimated dipole to quadrupole ratio. Third, data coverage also causes numerical issues related to the separation of the field into its internal and external contributions with respect to Mercury's surface. The numerically strong correlation between internal and external SH coefficients was in-depth investigated by Uno et al. (2009) in the case of MESSENGER's data. A more formal and general mathematical discussion about this separation problem can be found in Olsen et al. (2010).

The offset dipole hypothesis resorts to further explicit assumptions. One of them is that the magnetospheric current system is shifted northward. The position of the magnetic equator thus constrains the morphology of the internal (Anderson et al., 2012) and external field (Alexeev et al., 2010; Winslow et al., 2013; Korth et al., 2014), or both when a joint analysis is conducted (Johnson et al., 2012). This strong hypothesis stems from the observation that the location of the magnetic equator is statistically invariant between 1000 km and 5000 km altitudes (Anderson et al., 2011). Although a planetary magnetic field may indeed appear essentially dipolar by geometric attenuation with altitude, the best-fit position of the equivalent (axial and offset) dipole varies with the radius (or altitude) of the measurements for any field deviating from the pure dipole geometry (Lowes, 1994).

The apparently constant location of the magnetic equator with altitude may be altered by the fact that measurements are noisy and made at some distance from the planet, i.e., above 1000 km. Further complications arise in the case of Mercury and MESSENGER. First the magnetic equator is not crossed at lower altitudes. Second electric currents are present in the Hermean environment [e.g., Alexeev et al., 2010; Anderson et al., 2010, 2013, 2014] and require special care to select and analyze the measurements. One possible route to circumvent the lack of global coverage of measurements is to carry out regional analyses. Oliveira et al. (2015) for example proposed to model the measurements over the northern hemisphere by an equivalent layer of magnetic dipoles placed at depth in the Mercury's interior.

In this paper, we choose to apply the Revised Spherical Cap Harmonic Analysis [R-SCHA, Thébault et al., 2006] to derive a regional static magnetic field model from low-altitude measurements only ($\leqslant$1000 km). This regional modeling approach uses continuous mathematical functions and differs from the equivalent source dipole one. In depth details of the R-SCHA method can be found in Thébault et al. (2006), Thébault (2008). In the next section, we recall the key elements of the method. Because the R-SCHA method is a potential field method, we discuss and justify the assumptions and approximations made to tackle the issue of electrical currents crossing Mercury's exosphere. We then summarize the synthetic analyses that were conducted to demonstrate the proof of concept of the method in the case of MESSENGER. The regional modeling is applied to MESSENGER's magnetic field measurements from March 2011 until April 2015 in Section 4. The regional model is finally discussed together with its relationships to SH in the spectral and in the spatial domains.

2. Method

2.1. Mathematical formalism

The magnetic field model is derived under the assumption that the selected measurements are acquired within a portion of the spherical shell that is free of electric currents. This assumption is justified in Section 2.3. In the specific case of Mercury and MESSENGER measurements we solve the problem within a spherical cone that is coaxial with the planet's rotation axis. The source free domain is closed below and above by two spherical caps at radius $r = R_M$ and at $b = R_M + 1000$ km, the maximum altitude of the measurements considered in this study. The cone is closed laterally at colatitude $\theta = \theta_0$ and covers all longitudes φ. In the R-SCHA method, the magnetic potential V is the sum of V_1 and V_2 that are expressed in terms of the infinite series (Thébault et al., 2006)

$$V_1(r,\theta,\varphi) = R_M \sum_{m=0}^{\infty}\sum_{k=1}^{\infty}\left[g_{n_k}^{m,i}\left(\frac{R_M}{r}\right)^{n_k+1} + q_{n_k}^{m,e}\left(\frac{r}{R_M}\right)^{n_k-1}\right] L_{n_k}^{m}(\theta,\varphi), \quad (1)$$

$$V_2(r,\theta,\varphi) = R_M \sum_{m=0}^{\infty}\sum_{p=1}^{\infty} g_p^m R_p(r) M_p^m(\theta,\varphi), \quad (2)$$

where m, p and k are integer indices. In practice, the expansion series are truncated at some maximum degree $M_{\max}, P_{\max}, K_{\max}$, whose values depend on the resolution of the data. m is the order of the R-SCHA harmonics and is the analog of the order m in SH [e.g., De Santis et al., 1999]. The coefficients $\left(g_{n_k}^{m,i}, q_{n_k}^{m,e}, g_p^m\right)$ are the regional coefficients and the unknowns of the inverse problem. The superscript i and e stand for internal and external, respectively. $R_p(r)$ are the radial functions of the so-called Mehler basis functions with $M_p^m(\theta,\varphi)$ describing the horizontal spatial variations of this contribution. $L_{n_k}^m(\theta,\varphi)$ are the generalization of the Legendre basis functions involving the Schmidt quasi-normalized associated Legendre functions $P_{n_k}^m(\theta)$ of degree n_k and order m. Here, the degree n_k is real and depends on the index k, the order m, and the half-aperture θ_0 of the cone. It is asymptotically related to the horizontal spatial wavelength on the Mercury's surface by

$$\lambda \simeq 2\pi R_M / n_k. \quad (3)$$

The R-SCHA mathematical functions have some useful properties which are detailed below. First, the solution is complete so that any potential field can be represented with a unique set of regional coefficients. Second, the basis functions are orthogonal within the volume under consideration. This represents an advantage over the standard SH analysis that requires *ad hoc* regularization when measurements are available only over a portion of the sphere [e.g., Uno et al., 2009]. Modeling the magnetic field measurements with orthogonal functions further guarantees that the model is little dependent on the truncation $K_{\max}$ and $P_{\max}$ of the infinite series (Eqs. 1 and 2). This minimizes the numerical covariance between parameters, significantly reduces possible spectral aliasing, and leads to a numerically stable inverse problem. This latter property provides some confidence that the noise and/or non-potential sources should not contaminate or bias the model. The only numerical adverse effect of solving the problem on a regional scale is the possible occurrence of edge effects near the boundaries of the considered domain.

The dot products of the functions within a spherical cap surface $\partial\Omega$ at radius r also allow defining magnetic field power spectra. Because both potentials are series expressed in terms of the order m (Eqs. 1 and 2) the total power $E_{\partial\Omega}$ on any arbitrary spherical cap surface can be split order by order into the sum of $E_m^{\partial\Omega}$

$$E_{\partial\Omega} = \iint \nabla V . \nabla V \partial\Omega_c = \sum_{m=0} E_m^{\partial\Omega}. \quad (4)$$

This distribution of the energy among the orders m is referred to as the surface azimuthal power spectrum in the following. When the vector field averages out to zero within the volume, or when the field has angular spatial scales smaller than the half-angle θ_0,

the contributions from the Mehler functions (V_2) are negligible. In this case, the energy is mostly carried by the Legendre basis functions and we can reasonably approximate

$$E_{\partial\Omega} \simeq \iint \nabla V_1 . \nabla V_1 \partial\Omega_c, \tag{5}$$

and by reversing the order of summation

$$E_{\partial\Omega} \simeq \sum_{k=1} E_k^{\partial\Omega}. \tag{6}$$

2.2. Relations to global Spherical Harmonics

The degree n_k is asymptotically independent of m when $k \gg 1$ and is simply related to k (Robin, 1959)

$$n_k^a \simeq (k + 1/2)\frac{\pi}{2\theta_0} - \frac{1}{2}. \tag{7}$$

Vervelidou and Thébault (2015) derived a second power spectrum relating this degree n_k to a typical length scale such a λ (see Eq. 3). It is thus possible to group together the magnetic field contributions belonging to basis functions with similar numerical values of degrees n_k around the asymptotic expression n_k^a. This so-called horizontal spatial power spectrum can be compared to the global spatial Mauersberger-Lowes power spectrum (Lowes, 1966) derived in SH (Vervelidou and Thébault, 2015) although it is not equivalent degree by degree. For this reason, the n_k^a values are hereafter named the equivalent SH degrees.

Finally the regional parameters are analytically related to the internal g_l^m and external q_l^m SH Gauss coefficients with l and m the SH degree and order. For example, the so-called external R-SCHA coefficients are related to the SH Gauss coefficients by the expression (Thébault et al., 2006)

$$q_{n_k}^{m,e} = \sum_{l=m}^{\infty} \frac{(l+1)\left\langle P_{n_k}^m, P_l^m \right\rangle \left(1 - (R_M/b)^{l-n_k}\right)}{\left\| P_{n_k}^m \right\|^2 (n_k+1)\left((b/R_M)^{2n_k+1} - 1\right)} g_l^m + \sum_{l=m}^{\infty} \frac{l\left\langle P_{n_k}^m, P_l^m \right\rangle \left((R_M/b)^{l+n_k+1} - 1\right)}{\left\| P_{n_k}^m \right\|^2 n_k \left((b/R_M)^{2n_k+1} - 1\right)} q_l^m, \tag{8}$$

where the dot products between the Legendre functions are

$$\left\langle P_{n_k}^m, P_l^m \right\rangle = \int_0^{\theta_0} P_{n_k}^m P_l^m \sin\theta d\theta \tag{9}$$

and their norm

$$\left\| P_{n_k}^m \right\|^2 = \int_0^{\theta_0} P_{n_k}^m P_{n_k}^m \sin\theta d\theta. \tag{10}$$

Similar relationships can be written for the $g_{n_k}^{m,i}$ and g_p^m regional coefficients. A set of global internal and external SH coefficients can be estimated by numerical inversion of these relationships or by linear inversion of the regional magnetic field prediction within the cone. This, however, cannot be done in an unambiguous way as the given example shows the linear dependency of the regional external coefficients to both the internal g_l^m and external q_l^m SH global Gauss coefficients. This illustrates the classical problem in potential field methods to properly separate internal and external fields when the information (i.e., measurements) is available only over a limited area of the sphere. This issue is not specific to R-SCHA. Instead it arises because the exact separation between internal and external fields with respect to the planet's surface is possible only if magnetic vector measurements are available on a closed spherical surface (Backus et al., 1996). In the case of Mercury, we work over an almost complete hemisphere and we are close to the approximation $\theta_0 \simeq 90^\circ$. For such a spherical cap centered on the northern hemisphere we find that $n_k \simeq l$ and $\left\langle P_{n_k}^m, P_l^m \right\rangle = \left\| P_{n_k}^m \right\|^2$. Because the numerator $\left(1 - (R_M/b)^{l-nk}\right)$ further vanishes in Eq. (8) the expression in Eq. 8 reduces to

$$q_{n_k}^{m,e} \simeq q_l^m, n_k \simeq l \text{for} l - m \text{odd}.$$

A similar result can be obtained for the internal SH coefficients using [Thébault et al. (2006) their Eq. 28]. It results that, when analysing MESSENGER measurements with R-SCHA, the regional internal and external coefficients are also almost the analogues of the internal and external SH global Gauss coefficients for the $l - m$ odd terms. We note that the SH $l - m$ even terms are unconstrained by the measurements in the Northern hemisphere, as it will be discussed below. The R-SCHA modeling strategy is thus especially appealing, as it makes it possible to infer hypotheses on a global scale in SH from regional analyses.

2.3. Hypotheses and data selection

The vector magnetic field can be completely described in terms of the gradient of a scalar potential and the curl of a vector potential. The contributions carried by the curl of the vector potential are function of the electric current plus the displacement current according to the Ampère-Maxwell equation. They cancel out only in source free region. As a result, the internal field of Mercury is a potential field above the surface or actually above the surface of the dynamo generation region if one assumes that the mantle is weakly electrically conductive [see for instance Verhoeven et al., 2009 who computed synthetic electrical conductivity profiles for different scenarios of the mantle composition]. However, other fields created by currents in the hermean environment below or at the altitude of the spacecraft may bias the potential field representation.

A classical way to minimize the occurrence of currents and their effects on the internal field modeling is to rely first on a data selection procedure. One purpose of this selection is to reject data that agree the least with the source-free assumption. Features for which the temporal and spatial complexity are not compatible with the model parameters or the smoothing norm functions used for their mathematical representation in time and in space can also be a priori eliminated. Among the possible contaminating fields, the ones created by magnetospheric currents at altitudes above the magnetopause subsolar standoff distance [about 0.4 of Mercury's radius in the dayside, see Anderson et al., 2008] are particularly complex. Their large spatial scales indeed overlap with the internal planetary field of Mercury. To minimize them it is sufficient to select data measured within the magnetospheric cavity only, i.e., outside and possibly far from the magnetopause crossing and at magnetically quiet times. This data selection does not remove the poloidal fields generated by magnetospheric currents within the magnetospheric cavity, but these can be represented by relatively smooth and large spatial scale external harmonic functions which we use in this study. The global poloidal magnetospheric fields are thus not problematic provided that we coestimate internal and external fields.

Mercury has no ionosphere and its exosphere is essentially neutral (Slavin et al., 2007). There is thus no shell or layer of horizontal currents within the magnetospheric cavity. Compared to Earth, this situation considerably alleviates the problem of separating internal and external magnetic fields from space (Finlay et al., 2016).

A major source of concerns on Mercury is related to the magnetospheric currents that reconnect within the planet (Janhunen and Kallio et al., 2004) through Field Aligned Currents (FACs). These so-

called Birkeland currents at Mercury were first observed in the Mariner measurements (Slavin et al., 1997). They were more recently confirmed with an analysis of the MESSENGER's measurements (Anderson et al., 2014). In our approach, these currents are in principle the most problematic ones because their presence within the magnetospheric cavity is in contradiction with the source free method we apply.

Yet, the situation is maybe not so severe. During magnetically quiet times, the poloidal and toroidal magnetic fields generated by the FACs are in excess of 20 nT (Anderson et al. (2014), see their Fig. 2). However, toroidal and poloidal magnetic fields are by definition orthogonal (Backus et al., 1996). Only a fraction of these associated fields, the poloidal ones, may thus leak into the poloidal part of the regional model. Apart from transient perturbations, the remaining fraction of the 20 nT magnetic fields associated with the FACs are relatively fixed with respect to Magnetic Local Time (MLT) and exhibit a different polarity between the day and the night sides. They thus average out over one Mercury's solar day (about 176 Earth's days). In this study, we consider more than 8 solar days (about 4 Earth's years) of MESSENGER's measurements. This is a time span long enough so that it further minimizes the risk of strong contamination.

In order to further reduce this possible leakage which would be restricted to the polar area north of 60°N, we implement numerical safeguards in the inverse problem. Measurements are weighted according to their latitude by putting more constraint on low latitude than on high latitude measurements. We also apply an algorithm to iteratively reweight the data that may still be contaminated by significant transient magnetic field perturbations.

The only issue that cannot be resolved by the available measurements is currents generating quasi-static fields between the surface of the dynamo region and the orbit of MESSENGER. These contributions would be seen as internal fields and not separable from the internal field of the planet. This ambiguity, that arises also when fields are induced in the planet by external fields is ubiquitous in planetary magnetism (Olsen et al., 2010) and can be addressed only by time-varying field analyses.

We use the latest MESSENGER calibrated magnetic field measurements (MESSENGER Data Release 15, version V08) acquired during more than 8 Mercury solar days from 23 March 2011 until 30 April 2015. We apply a proxy defined by Oliveira et al. (2015) to identify and reject measurements with high-frequency variations which are usually present outside the magnetosphere and which disappear inside the magnetopause. This proxy allows us to identify and to select for each orbit only the measurements within the magnetospheric cavity. In addition, we keep only the measurements acquired below 1000 km altitude. This maximum altitude further aims at excluding data too close to the day side magnetopause that may have large spatio-temporal variability. The selected orbit portions correspond to reduced external field perturbations. All selected data below 1000 km altitude are north of 5° latitude. Therefore, we set the half-aperture of the cone to $\theta_0 = 85°$. The cone is aligned onto Mercury's axis of rotation and covers almost the entire Northern hemisphere. A full azimuthal coverage in the Mercury Body Fixed (MBF) coordinate system is completed every sidereal day on Mercury (about 56 Earth's days). The geographical coverage within the cone in the MBF reference frame is therefore very dense. Due to the spin orbit 3:2 resonance on Mercury, all MLT are surveyed after 3 days or 2 years, which corresponds to 1 solar day. The coverage in MLT is sufficient to average out (in principle) the external field contributions which are more or less static in the Mercury-centric Solar Orbital (MSO) reference frame. The median and mean altitudes of the measurements are 500 and 530 km, respectively. The radial distribution is dense, but the low latitude measurements are at higher altitudes, with a median altitude equal to 700 and 450 km south and north of 45°N, respectively. This data selection protocol generates a dataset of 1,675,748 data triplet (5,141,166 vector field components).

3. Synthetic analysis

In this section we carry out a simple end-to-end synthetic analysis which consists in first computing a synthetic magnetic field in SH on the location of the selected MESSENGER data as described above and then in estimating the SH Gauss coefficients from the regional model. We attempt to simulate a realistic internal magnetic field at Mercury. For this, we use the SH internal Gauss coefficients estimated by Anderson et al. (2012) see their Table 4] for the zonal terms ($m = 0$) from degree $l = 1$ to 4 (right column of Table 1). The magnetic field contributions of the other SH coefficients up to degree 10 are assumed to amount to 20 nT Root Mean Square (RMS) in total on Mercury's spherical surface. Their individual values are drawn from a random Gaussian distribution and the energy is distributed equally over the SH degrees. For the magnetospheric field, we simulate a 88-day temporal variation (1 Hermean year) as a function of the heliocentric distance. The magnetospheric field, simply represented in SH by the q_1^0 coefficient, is assumed to be stronger at the perihelion and weaker at the aphelion. We add to this periodic variation of the external field a 88-day variation with random amplitude in order to simulate changes of the solar wind plasma (see Fig. 1). For the simulation of the external field we do not consider other source fields such as FACs. The synthetic magnetic field vector components are computed at the location of the selected MESSENGER's measurements. We further add a random noise with a standard deviation of 20 nT to simulate data errors and to test the numerical stability of the solution with downward continuation to the core-mantle boundary. The synthetic field model contains a signal up to SH degree 10 but we expand the R-SCHA series to equivalent R-SCHA degree 18 in order to investigate the propagation of the noise within the regional coefficients at higher harmonics. This also helps to identify possible spectral aliasing. We also coestimate the external part of the regional basis functions to illustrate and quantify the leakage of global external field into internal and external regional coefficients when a cone of 85° half-aperture is considered. The infinite series in Eqs. (1) and (2) are truncated to $K_{max} = 18, M_{max} = 18$ and $P_{max} = 4$. With these truncations, the conditioning of the inverse problem is satisfactory and the inverse matrix is essentially diagonal thus showing that the basis functions, given the real data distribution, are numerically close-to-orthogonal. The maximum theoretical horizontal spatial resolution of the model is about 830 km on the Mercury's mean spherical surface.

Table 1
Estimated SH Gauss coefficients for the internal and external parts (in unit of nT) for different degrees l and orders m. The input model used is shown for comparison in the right column. External SH Gauss coefficients of degree larger than 1 are not estimated.

Internal	Case 1	Case 2	Input model
g_1^0	−213.2	−189.7	−190.0
g_1^1	−1.7	1.6	0.1
h_1^1	1.5	0.3	0.5
g_2^0	−155.7	−74.7	−74.6
g_3^0	159.5	−24.2	−22.0
g_4^0	−131.4	–	−5.7
g_5^0	73.1	3.4	8.3
External			
q_1^0	−41.2	−40.4	−40.0
q_1^1	0.3	0.2	0.0
s_1^1	−0.1	−0.1	0.0

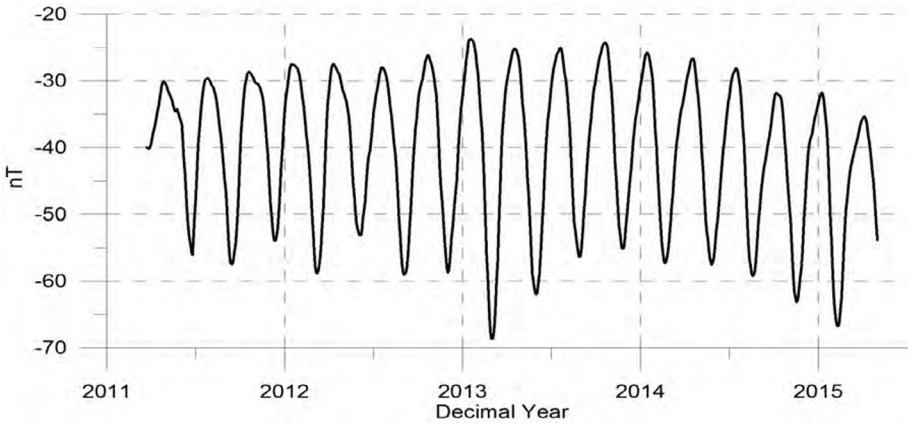

Fig. 1. Simulated temporal variation of the external Gauss coefficient q_1^0 (in unit of nT) as a function of the heliocentric distance of Mercury over the entire MESSENGER's mission lifetime. The mean value is $q_1^0 = -40$ nT.

In order to derive a solution in agreement with the dot product in the cone (see Eq. 9) we weight the measurements by $\sin\theta_i$, where θ_i is the colatitude of each vector measurement i. This weight also mitigates the possible contamination of the model by magnetic field associated with the FACs. We further use an Iteratively Reweighted Least Squares (IRLS) procedure to identify and underweight the outliers. The weights entering the IRLS calculation are allocated by a hypothesis on the error distribution known as the Huber distribution (Huber, 1981). The data departure from the best estimation of the mean model is chosen as a compromise between a Gaussian distribution within one standard deviation of the misfit function and a longer-tailed Laplace distribution otherwise [see for example Thébault et al., 2015, their Eq. 15]. This procedure is designed to minimize the possible bias introduced by time-varying external magnetic fields and/or discrepant measurements.

The standard deviation between the noisy measurements and the regional model is 20.02 nT, 20.00 nT, and 20.02 nT respectively on the North (X), East (Y), and Vertical (Z) spherical components. This is consistent with the amount of Gaussian random noise added to the synthetic data and the magnitude of the temporal synthetic external field variations. The model and the data correlate to 97% and the mean difference is centered on zero, indicating no misfit bias. Fig. 2 represents the noise-free radial component of the internal synthetic SH model at 400 km depth, which is the commonly accepted depth of the core mantle boundary (CMB) at Mercury (Hauck et al., 2013; Rivoldini and Van Hoolst et al., 2013). The vertical component predicted by the R-SCHA internal model at the CMB is sketched in the middle and the differences between the input and predicted fields are shown on the right panel. We confirm that the R-SCHA model is stable and noise-free. It can further be downward continued to Mercury's CMB in spite of the large mean/median distance between the measurements and the CMB. The horizontal components (not shown) indicate a similar level of agreement. The most important feature in the residual maps is the relative increase of small scale residuals at the lateral (southern) boundary. This is due to well-known edge effects occurring when modeling a global field on a small portion of the sphere. Keeping this limitation in mind, the RMS difference between the initial SH and the resulting R-SCHA models estimated from the noisy synthetic measurements is about 60 nT (10%) for the X, 20 nT for the Y (20%), and 60 nT (9%) for the Z components at the CMB.

We show in Fig. 3 the R-SCHA azimuthal power spectrum given by Eq. (4) at the CMB. The spectrum informs us about the distribution of the magnetic energy among the orders m and will be used hereafter to compare the energy carried by the zonal and non-zonal terms. As expected by construction of the synthetic SH model, the resulting mean R-SCHA model is mostly zonal. The azimuthal distribution of the SH model (for the whole sphere) is shown for comparison. There is a good agreement between the regional and the global azimuthal spectra. The small differences arise because the R-SCHA azimuthal power spectrum describes

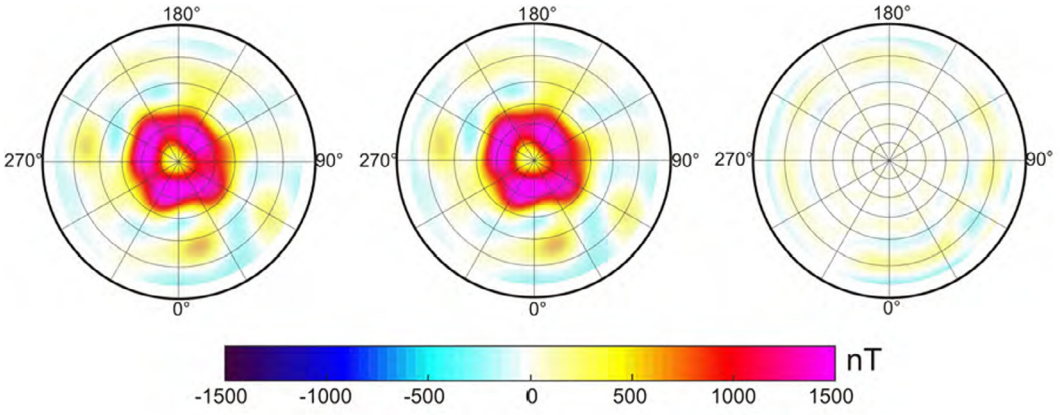

Fig. 2. Left: vertical component of the synthetic SH model computed at the core mantle boundary of Mercury assumed to be at 400 km depth; Middle: vertical component of the R-SCHA model at the CMB; right: difference between both vertical components.

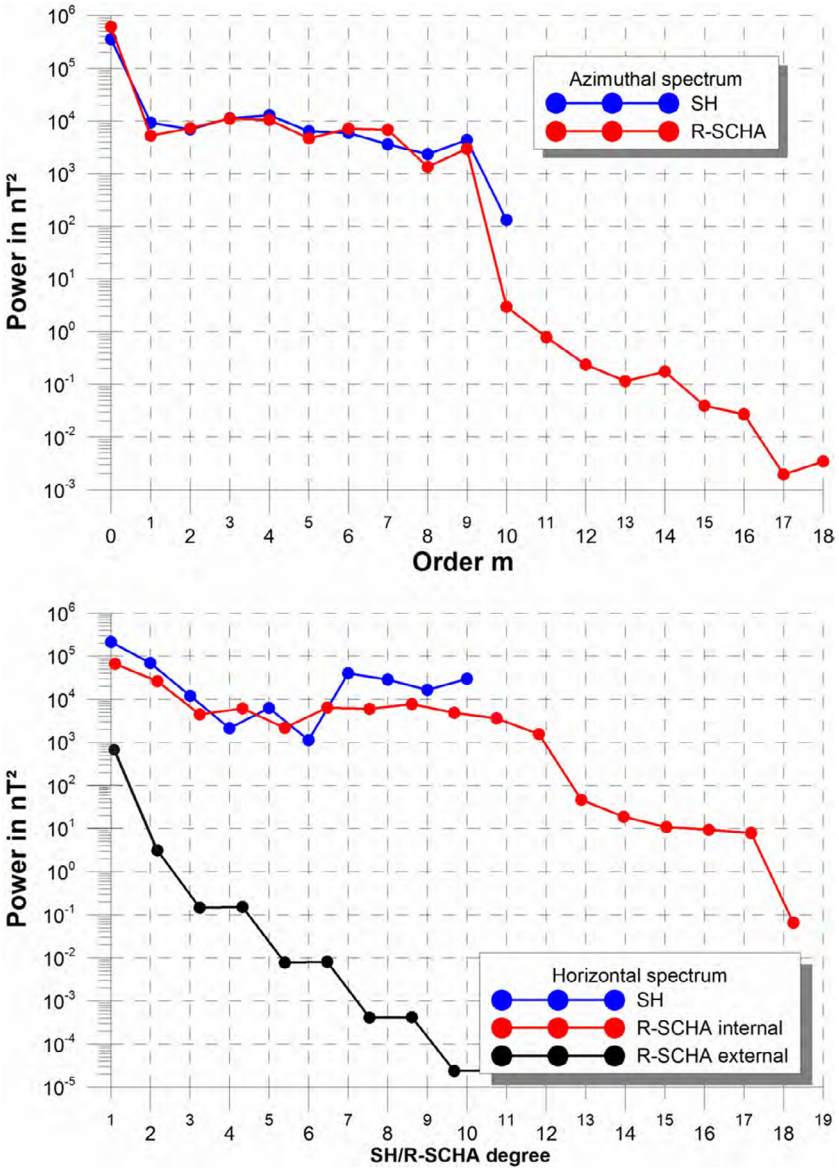

Fig. 3. Top: azimuthal power spectra of the synthetic SH (blue) and the R-SCHA (red) models at the CMB; bottom: horizontal spatial power spectrum of the SH (blue) and the R-SCHA (red) models at the CMB. Full symbols show the value of the order m and degrees (see text for details). (For interpretation of the references to colour in this figure legend, the reader is referred to the web version of this article.)

the mean square field over a portion of the northern hemisphere while the SH azimuthal spectrum characterizes the mean square field over the entire sphere. We also compute with the Eq. (6) the spatial power spectrum at the CMB and split its contributions into the internal and external terms. As indicated above, the degrees n_k values are real, not integer. The external regional coefficients above R-SCHA degree 1 are not zero, which was expected from the above discussion concerning the internal/external separation problem. However, the power spectrum of these contributions is at least four orders of magnitude lower than the power spectrum of the internal regional coefficients. At the CMB, the leakage of the internal field into the external R-SCHA coefficients amounts to less than 5 nT RMS. This is a value smaller than the difference between the SH and the R-SCHA model at the CMB due to downward continuation issues. The difference between the R-SCHA and SH spatial power spectra is the indication that the regional spatial power spectrum does not carry alone the full signal. The Legendre basis function carry 96% of it while 4% is carried by the Mehler basis functions. An important feature emerging from the azimuthal and the spatial power spectra is the cutoff around the order 10. This corresponds to the maximum spatial expansion of the synthetic SH model. Because the R-SCHA and SH degrees are not strictly equivalent representation of the field, the cutoff is slightly shifted towards larger R-SCHA degrees [see also Vervelidou and Thébault, 2015; Maus, 2008].

This simulation demonstrates the consistency and the usefulness of the regional model to infer some general properties of the magnetic field at different altitudes and depths (such as the distribution of the energy among orders and degrees, for example). However, a global SH model is useful for planetary scale applications. We thus attempt to convert the regional model into a global SH model. When doing so, it is important to stress again that the solution cannot be unique. When measurements are available only over the northern hemisphere, only $l-m$ odd SH terms form an orthogonal basis and are therefore mathematically separable. This implies that introducing the $l-m$ even terms in the SH analysis causes covariance among all coefficients. This covariance between coefficients represents a serious problem. It may be responsible for

numerical instabilities which may translate into magnetic energy transfer from some coefficients into some others [e.g. Korth et al., 2014; Uno et al., 2009]. As a result, the analysis of the estimated model in the spectral domain should be done with care.

Yet, the covariance between the coefficients can be minimized with a careful selection of the coefficients best representing the magnetic field characteristics. This implies that the truncated global magnetic field model in SH is not as complete as the regional one. In addition, the estimated terms may carry some energy belonging to non-estimated terms. This spectral leakage, or aliasing, is commonly observed in modelling the Earth's magnetic field with truncated SH functions [e.g. Baerenzung et al., 2014]. Pre-MESSENGER models of Mercury's magnetic field coevaluating the zonal dipole and quadrupole terms are suspected to be aliased in a similar way [e.g., Connerney and Ness, 1999 their Fig. 5]. Choosing the most relevant SH coefficients to represent the measurements while minimizing the covariance between them is no trivial matter. For example, one of the most striking features of the Mercury's field are the large scale and essentially zonal structures and the Northward shift of the magnetic equator. The SH models of (Anderson et al., 2008) and (Johnson et al., 2012) are strongly constrained by this observation. Note that the $l-m$ odd zonal terms are symmetric with respect to the geographic equator. They cannot reproduce alone this apparent magnetic field asymmetry. As a consequence, at least one $l-m$ even term must be added in the SH analysis in order to derive a model that mimics this important feature. However, this is done at the cost of degrading the estimation of the $l-m$ odd terms. We verify numerically these general considerations. The regional synthetic model is converted into two sets of SH Gauss coefficients. The first set (case 1) of Gauss coefficients consists in the full internal dipole term ($l=1$) and all zonal terms from degree 2 to 5. The second set (case 2) includes the full dipole terms ($l=1$), the zonal and l odd terms, and the g_2^0 coefficient. For both models, we also coestimate the external dipole term ($l=1$). The difference between the two sets of estimated SH models is thus the g_4^0 coefficient. Higher degree terms are not considered because they are not meaningful due to covariance issues. The results are shown in Table 1 together with the input SH model. The case 2 coefficients are well correlated with those of the input model while the case 1 suffers from numerical instabilities. Better performance could have maybe been obtained by adding a priori regularization or assumption but our intention is to illustrate only the covariance issue without regularization. The exact separation between internal and external fields is numerically not tractable due to incomplete coverage [e.g., Olsen et al., 2010]. However, in both cases we note that the estimated external dipole terms are consistent with the value of the synthetic input model. We derive two main conclusions from these synthetic tests. First, including $l-m$ even terms introduces errors on all harmonics. This can however be minimized by considering only the g_2^0 coefficient. Second, a first order internal/external field separation is achievable with our approach. We stress out that these conclusions are valid for the assumptions we made here considering the field geometry and the measurements distribution. In the following we consider a SH global model without the g_4^0 coefficient. This differs from the model of (Anderson et al., 2011) and (Johnson et al., 2012). This global SH model is based on a R-SCHA model which is presented in the next section.

4. Application to MESSENGER data and discussion

4.1. Misfit to the measurements

The MESSENGER's vector measurements are modelled regionally with the same degree truncation as discussed previously. The misfit between the vector field measurements and the model is about 29 nT (Table 2) with the model explaining more than 97% of the magnetic field signal at altitudes lower than 1000 km. The nearly zero mean residual distribution for each component indicates that no significant static field contribution is missed by the regional model.

We display in Fig. (4) the differences between the field intensity of the measurements and that predicted by the regional model as a function of the longitude, the latitude, the altitude, the epoch and the local time. In each case, we also display a 6th degree polynomial fit of the residuals (red line). This polynomial has no physical significance but helps us to identify the occurrence of a general trend between the residuals and the position in space and/or time of the data. We observe comparatively larger scatter in the residuals at large latitudes compared to low latitudes. A similar observation is made at high altitudes (above 350 km) compared to low altitudes. High latitude larger differences can be attributed to FACs and/or to the fact that the measurements are underweighted. High altitude differences can be explained by the proximity of the data to the magnetopause and a larger contamination by small scale transient external fields.

More importantly, the residuals are correlated with the time. There is a 88-day modulation of the residuals (one Hermean year) and a significant year to year variability. The residuals are also clearly correlated with the local time. They are stronger and more scattered during day than during night times. We also detect evident outliers in the dataset that a posteriori justify the use of the robust weighting scheme in the inverse problem. The focus of the present work is not on the time varying external field. However, we note that a significant fraction of the residuals (or non-modelled features) can be related to the day of year of MESSENGER around Mercury and to the local time. The model we derive has to be seen as a time-averaged regional model of the Hermean magnetic field. These residuals further show that the time-varying external magnetic field around Mercury does not enter the model.

4.2. Spectral analyses

The surface azimuthal power spectrum (Eq. 4) is computed at three altitudes (Fig. 5-top). At 500 km (the mean altitude of the measurements) the zonal terms carry 99% of the signal. At the surface of Mercury the power spectrum indicates that the RMS total field is 411±23 nT. The zonal terms represent 99% of the total signal. About 1% RMS (less than 25 nT) is distributed on non-zonal terms. The behavior of the azimuthal power spectrum with downward continuation to the CMB does not exhibit unrealistic values for the large orders terms and seems converged. At the CMB the RMS field is about 752±43 nT and remains zonal at 98%. The regional model confirms that the Hermean magnetic field is strongly symmetric with respect to the planet's spin axis which is a particularly intriguing feature.

The Legendre functions (V_1) account for more than 96% of the field RMS at Mercury's mean surface, the estimated CMB, and the mean altitude of MESSENGER's data. We therefore neglect for a while the contribution of potential V_2 (Eq. 2) and we compute with

Table 2
Misfit statistics: standard deviation (std), mean residuals (<residuals >) and correlation R between the model and the measurements for the Vertical (Z), the North (X) and the East (Y) field component.

Component	std (nT)	<residuals> (nT)	R
$Z=-B_r$	26.4	0.1	0.98
$X=-B_\theta$	31.1	−0.2	0.88
$Y=B_\phi$	34.0	−0.2	0.12
All vector components	30.6	−0.1	0.97

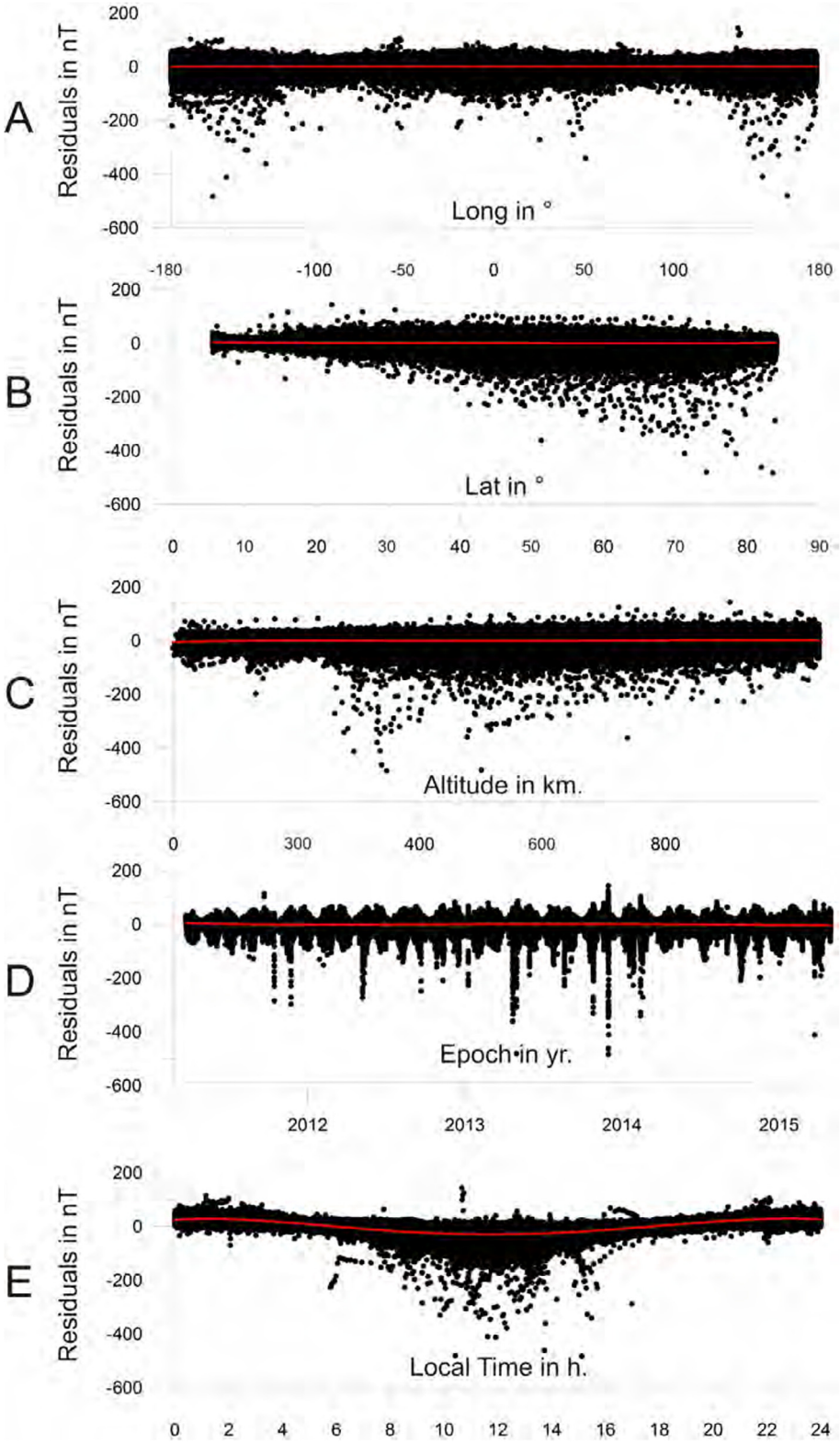

Fig. 4. Intensity misfit between the MESSENGER measurements and the R-SCHA model as a function of the geographic longitude (A), the latitude (B), the altitude (C), the epoch (D), and the local time (E). The red curves are the respective best fit of a polynomial of order 6 (see text for details).

the Eq. (5) the horizontal spatial power spectra at various radii in Fig. (5-bottom). We display the power spectra of the internal and external contributions separately. The regional degrees n_k^a (Eq. 7) larger than 2 carry 16%, 5%, and 3% of the signal at the CMB, the surface and 500 km altitude, respectively. We also note that the external field is mostly present on spatial scales larger than about 7700 km (up to equivalent degree $n_k^a \simeq 2$) and that smaller scale contributions are negligible.

It has been proposed that the magnetic field spectrum is flat on the CMB (Backus et al., 1996), in particular its non-zonal part

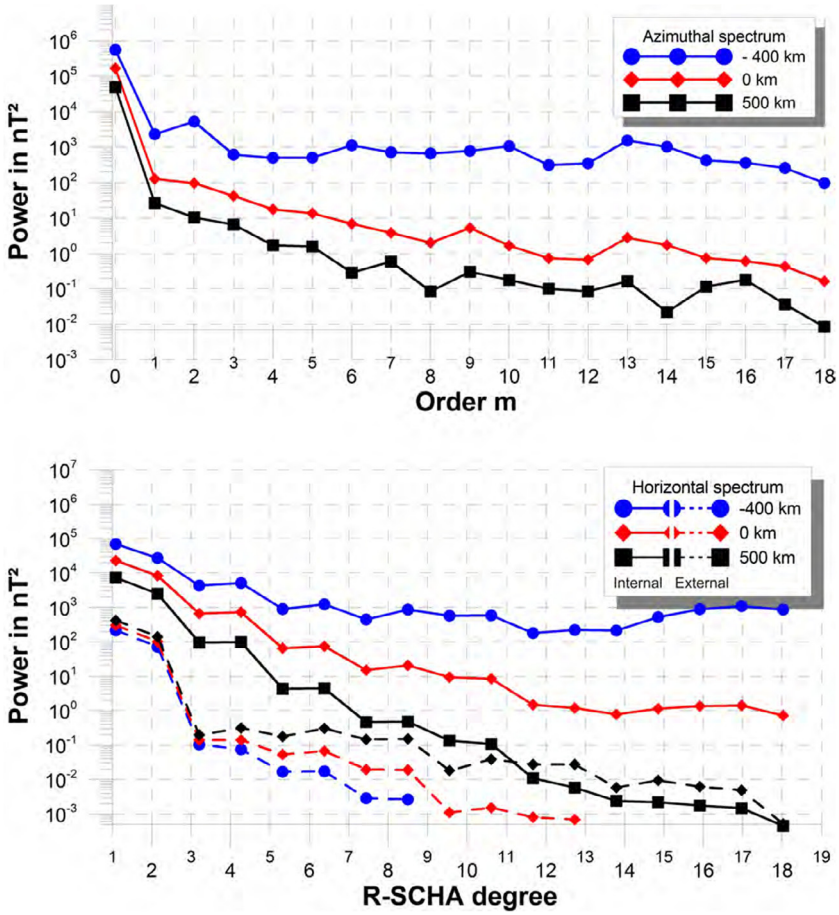

Fig. 5. Top: azimuthal power spectra of the R-SCHA model at the CMB (blue), on Mercury's mean surface (red) and at the mean altitude of MESSENGER's measurements (black); bottom: horizontal spatial power spectrum of R-SCHA models at the CMB (blue), at Mercury's mean surface (red) and at the mean altitude of the MESSENGER's measurements (black). Solid lines show the spectra of the internal parameters and dotted lines show the spectra of the external parameters. (For interpretation of the references to colour in this figure legend, the reader is referred to the web version of this article.)

(Langlais et al., 2014). Here, the general shape of the power spectrum at 400 km depth is decreasing up to equivalent degree 13 but is in general agreement with the estimated depth of the CMB inferred from gravity field measurements (Hauck et al., 2013; Rivoldini and Van Hoolst et al., 2013). There is a small rise of the power spectrum at the CMB beyond R-SCHA degree/order 13. These degrees have a rather flat contribution on Mercury's mean surface. They could be interpreted as the signature of a magnetic crust similar to what is observed on Earth around SH degrees 13–15 [see Thébault et al., 2010, for a review]. In order to estimate what might be the crustal field contribution, we assume that the magnetic crust is 35 km thick (Padovan et al., 2015) and consider that the TRM susceptibility of the rocks is about 0.01 SI (Johnson et al., 2015). A model for the crustal field power spectrum (Thébault and Vervelidou et al., 2015) indicates that the crustal field at Mercury's mean radius should not exceed 1–5 nT RMS. This is comparable to the contributions of R-SCHA degrees 11 to 18 (about 2.3 nT RMS). However, such a value is much smaller than the misfit between the regional model and the measurements. The Student's t-test on the estimated parameters also indicates that more than 85% of the regional coefficients at equivalent degrees n_k^a larger than 11 are statistically not significant at 95%. Their omission in the regional model would not statistically degrade the representation of the field.

A visual observation of Mercury's surface suggests that a variety of geological processes such as volcanism and cratering could have produced magnetization contrasts as is the case on Mars and the Moon [e.g., Langlais et al., 2010]. Johnson et al. (2015), Hood (2015a,b) analysed the lowest altitude MESSENGER's measurements and detected only very small scale magnetic crustal signatures so far. These observations are in contradiction with a hypothetical existence of large scale and coherent magnetic crustal structures starting at equivalent degrees larger than 11. We conclude that the magnetic field contributions at degrees and orders larger than 11 are caused by the amplification of noise with the downward continuation of the model and that there is no evidence of large spatial scale (>850 km) remanent crustal field at Mercury.

4.3. Physical domain analyses

We display the magnetic field model at the CMB and the Mercury's mean spherical surface over the Northern hemisphere in Fig. (6). This model includes the Mehler contributions and all internal and external regional field contributions up to equivalent R-SCHA degree 11 (see previous subsection). The magnetic field is strongly axisymmetric. The North dip pole is located at $87^\circ N, 94^\circ W$. The most striking feature in these plots is the absence of small scale structures at the CMB. This observation is not novel but relied so far on SH models truncated to very low degrees and orders. The synthetic example discussed above (Fig. 2) shows that even a weak contribution of 20 nT RMS distributed randomly among the Gauss coefficients is sufficient to produce a model with small scale structures clearly apparent and detectable at the CMB.

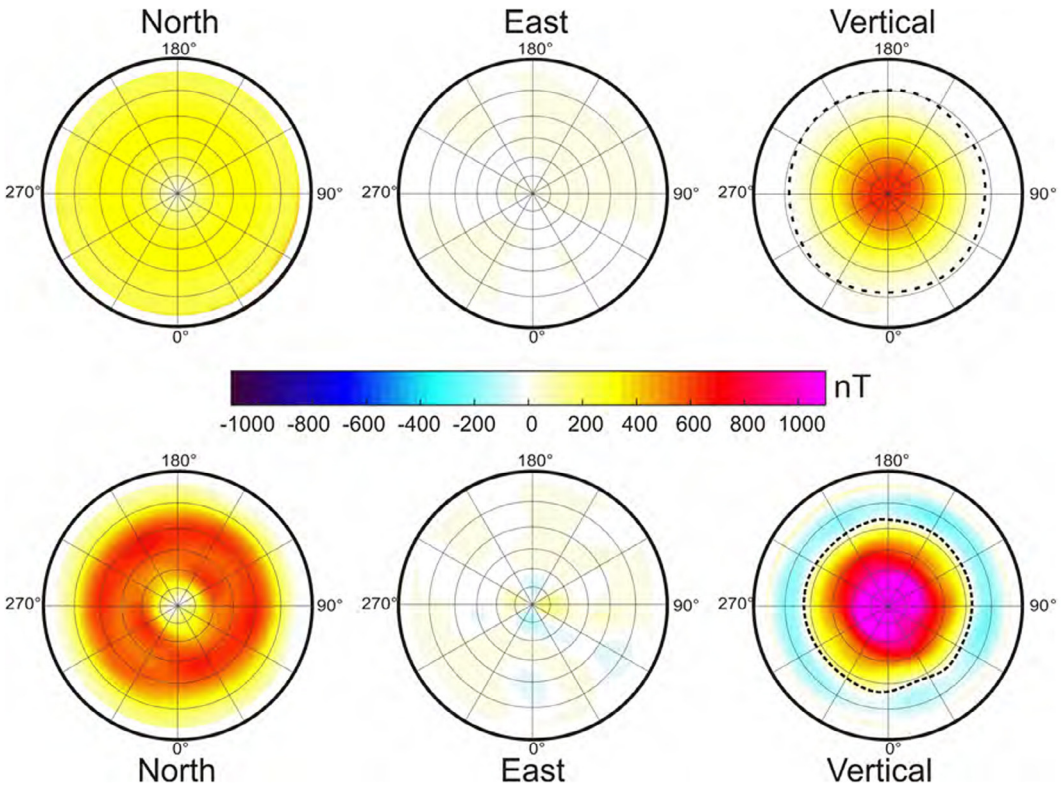

Fig. 6. Top: Magnetic field components of the internal and external R-SCHA model at the Mercury's mean surface over the Northern hemisphere. Bottom: same as on top but at 400 km depth. The dotted lines in the rightmost column indicate the location of the estimated magnetic equator.

Here, what is observed is a large scale, zonal, and smooth Hermean magnetic field.

The absence of small scale structures confirms that the model is stable and not strongly contaminated by noise or possible small scale external fields. In particular, there are no signature of the magnetic field created by FACs near the Mercury's northern magnetospheric cusp or above $60^{\circ}N$ in any component of the model. The only small scale structures observed at the CMB on the Y component near the pole can be attribute to the 10°polar gap in the measurements. The absence of signature from FACs is further confirmed in Fig. (7) where internal Legendre and Mehler contributions are plotted separately from the external field contributions at the CMB. The external field contribution is essentially large scale as inferred from the spectrum Fig. (5-bottom).

4.4. The magnetic equator

The classical definition of the magnetic dip, or magnetic equator, is the region where the magnetic field inclination $I = atan(Z/H)$ is zero, with H being the intensity of the horizontal magnetic field and Z its vertical component [e.g., Thébault et al., 2015, their Eq. 5]. For simplification here we identify the magnetic dip equator as regions where the absolute value of the vertical magnetic field component (Z) is less than the arbitrary value of 2 nT. This definition implies that the Mercury body-centered radial component is zero at the equator. This differs from the definition advocated by (Anderson et al., 2011) who choose to identify the magnetic equator from the zero crossing of the cyclindrical radial component of the magnetic field.

The regional model computed at the location of all selected measurements predicts the location of the magnetic equator around latitude $14.9^{\circ}N \pm 2.2^{\circ}$on average within the cone. This estimate is in close agreement with the mode of the magnetic equator distribution found at latitude $15.8^{\circ}N \pm 5.8^{\circ}$ that is estimated from the vertical magnetic field of the MESSENGER measurements selected for this analysis. Here the mode of the distribution is preferred over other statistical averages such as the mean or the median because the real dip equator distribution is skewed toward northern latitudes at all altitudes (see the Fig. 8). The location of the magnetic dip equator varies with respect to the altitude in the spherical MBF reference frame and we verify that the mode of the real distribution (shaded grey in Fig. 8) is well predicted by the R-SCHA model (black curve). The location of the dip equator is better constrained by the measurements between 250 and 800 km. The uncertainty of its numerical estimation increases at larger altitudes where the effects of the dynamic magnetospheric fields are more prominent.

Even though global internal and external contributions can only be approximately separated with the regional model, we also display in Fig. 8 the magnetic dip equator inferred from the internal (red curve) and external (blue curve) regional parts. The 2σ error bars of the internal and external field components start overlapping from 900 km altitude. They intersect around 1050 km altitude ($1.43R_M$), where they predict a dip equator at the same average latitude of about $11.5^{\circ}N \pm 2.0$. This feature is consistent with the average location of the solar wind standoff distance at Mercury estimated at $1.41R_M$ by Johnson et al., 2012) and compares well with the estimates of Zhong et al. (2015), between $1.38R_M$ and $1.65R_M$ at aphelion and perihelion, respectively. As shown in Fig. 8 (yellow curve), this estimate is also in agreement with the magnetic dip equator estimated to be at $11.9N \pm 0.3$ at $1.38R_M$ at high altitudes in the SH model coefficients of Anderson et al. (2012). Finally, it is also consistent with the expectation that the shape of the magnetosphere should be symmetric with respect to the internal magnetic field at high altitudes (Anderson et al., 2011; Anderson et al., 2012; Johnson et al., 2012).

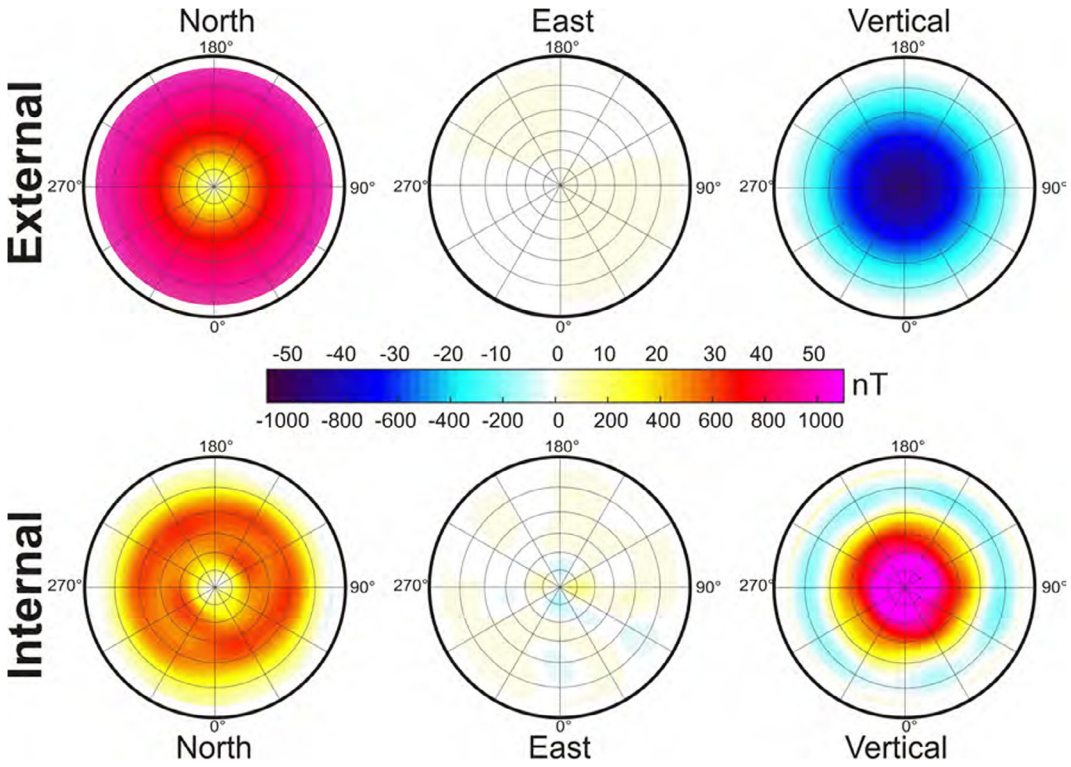

Fig. 7. Separation of the full model displayed in the Fig. (6) at the CMB into external (top) and internal (bottom) regional contributions for the North (left), East (center) and vertical (right) components. Note that the labels on the colorscale are different for the external and internal parts. (For interpretation of the references to colour in this figure legend, the reader is referred to the web version of this article.)

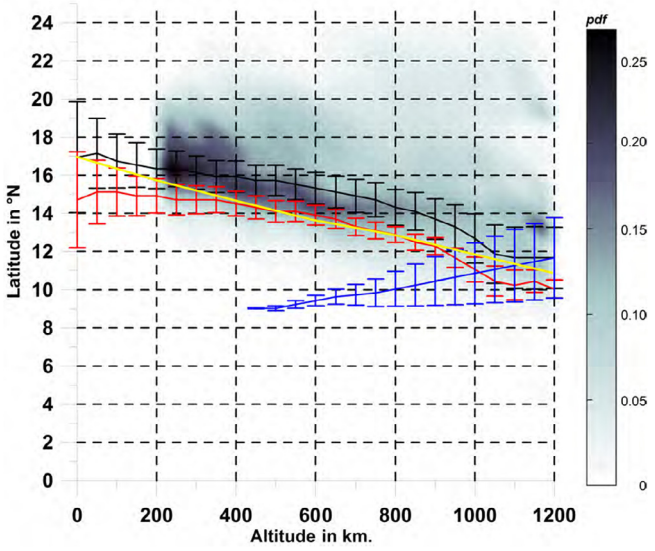

Fig. 8. North geographic latitude of the magnetic dip equator as a function of the altitude between 0 and 1200 km altitude estimated from the measurements (probability density in grey), from the full regional model (in black), from its internal component (in red) and from its external component (in blue). The error bars are the 2σ estimates. The yellow curve shows the location of the magnetic equator estimated from the SH model of Anderson et al. (2012). (For interpretation of the references to colour in this figure legend, the reader is referred to the web version of this article.)

5. Spherical harmonics models

We finally transform the regional model into a truncated global SH model. We estimate only the low degree coefficients that are the least correlated over the northern hemisphere as discussed in Section (3). Internal and external Gauss coefficients are considered. We compute three different global SH models. The first one (M1 in Table 3) is derived using only the internal contributions of the regional model. This model should thus be associated with very low external field Gauss coefficients provided that the regional model separation into its internal and external contributions in Fig. (7) is satisfactory. The second inversion (M2) uses all contributions of the regional model. The third model (M3) uses the same contributions as M2 but is derived after putting 20 times more weight on the measurements located around the magnetic dip equator (defined as the region where the vertical component $|Z|<$ 2 nT). The last column of Table (3) shows the values of the SH coefficients provided by Anderson et al. (2012) for comparison. This model is denoted the MA model hereafter. The standard deviation between the regional model and the M1, M2 and M3 truncated SH models is about 8.5 nT in all three cases with a small bias of 0.5 nT in the mean residual. A small bias in the residual indicates that the model truncated to low degree do not account for all the spatial structures that are depicted by the high resolution regional model. The low value estimated for the external SH coefficient of model M1 ($q_1^0 = 2.8$ nT) provides some confidence that the regional modelling approach indeed separates the field into internal and external contributions. The internal SH coefficients of model M1 and M2 are of comparable magnitude even though they are estimated from two different contributions of the regional model. These two models, and in particular the M2 model, are significantly different from the model MA for which the dipole to quadrupole ratio is about 0.4. The model M2 exhibits a smaller ratio of 0.27. The energy distributes differently among the SH degrees as model M2 has significantly more power on the octupole term and less power on the quadrupole term than the MA model. Interestingly, the three models provide the same esti-

Table 3
Estimated SH Gauss coefficients for the internal and external parts (in unit of nT) and dipole tilt (in unit of °). Three models are estimated. M1 is derived only from Mehler and Legendre internal regional contributions. M2 is derived from the full regional model and M3 is derived from the full regional model after putting more constrain on the magnetic dip equator. The coefficients of model M4 provided by Anderson et al. (2012) are shown for comparison. The error bars are the 3σ standard estimates.

Internal	M1	M2	M3	M4
g_1^0	−213.2 ± 6.0	−213.6 ± 6.0	−198.8 ± 6.9	−190 ± 10
g_1^1	1.2 ± 0.4	0.9 ± 0.4	0.9 ± 0.9	n/a
h_1^1	1.6 ± 0.8	1.5 ± 0.8	1.8 ± 0.9	n/a
g_2^0	−56.5 ± 5.5	−57.7 ± 3.7	−77.6 ± 5.9	−74.6 ± 4.0
g_3^0	−34.0 ± 3.5	−35.8 ± 3.5	−20.6 ± 5.9	−22.0 ± 1.3
g_5^0	2.7 ± 0.8	2.1 ± 0.8	0.6 ± 0.9	n/a
External	–	–	–	–
q_1^0	2.8 ± 1.2	−39.7 ± 1.2	−36.7 ± 1.3	n/a
q_1^1	0.3 ± 0.4	0.1 ± 0.4	0.2 ± 0.6	n/a
s_1^1	−0.1 ± 0.4	−0.1 ± 0.4	−0.2 ± 0.6	n/a
g_2^0/g_1^0 ratio	0.27	0.27	0.39	0.39
g_3^0/g_1^0 ratio	0.16	0.17	0.10	0.12
Dipole tilt	0.6	0.6	0.6	0.8

mation of 0.6° for the mean dipole tilt. The results obtained for model M3 shows the importance of putting more weight on the location of the magnetic dip equator than elsewhere. Therefore, the observed difference in the Gauss coefficients between M2 and MA could be explained by this strong constraint used in the derivation of the MA model (Anderson et al., 2012).

6. Conclusion

In this paper we derived a regional model of the Hermean magnetic field using a regional modelling technique and a selection of the MESSENGERs measurements within the magnetospheric cavity from 2011 until 2015. The model confirms most of the structures observed at Mercury at high altitudes. The complete lack of small scale structures at the top the core is the most striking feature confirmed by this study. If Mercury sustains an active dynamo within its entire outer liquid core it should exhibit small scales magnetic field structures at the CMB. This complete absence of faint structures as well as the decreasing shape of the regional power spectrum at the CMB are strong arguments in favor of the possible existence of a stratified layer at the top of the core that would filter out smaller scales (Christensen, 2006). This assumes, of course, that the observed field is generated by a deep-seated dynamo. This characteristic is not an artefact introduced by some truncated SH representation but a genuine feature of the magnetic field. We also show that the transformation of the regional model into SH Gauss coefficients is not unique because of parameters covariance. This limitation is caused by the distribution of magnetic field measurements available only over the northern hemisphere of Mercury. As a result, the estimated SH models are necessarily hypothesis-dependent. For example, the truncated SH model of Anderson et al. (2012) is predominantly constrained by the location of the magnetic dip equator measured by high altitude measurements. This constrain seems to have a significant impact on the estimated ratio of the zonal dipole and quadrupole SH terms.

Our results illustrate that if the co-estimation of the zonal internal quadrupole and the external dipole terms are important to preserve the most robust features detected by the MESSENGER's measurements, a different picture of Mercury's magnetic field can be obtained in SH by relaxing this constrain. In such a case, the maximum likelihood SH model indicates that the axial quadrupole to axial dipole ratio is significantly reduced from 0.4 to 0.27. This result could broaden the class of acceptable dynamo regimes for Mercury by perhaps alleviating the need for heterogeneous heat flux at the CMB (Cao et al. et al., 2014; Wicht and Heyner, 2014). The model of Anderson et al. (2012) is therefore probably a suitable model to estimate the location of the magnetic dip pole but, in our approach, is statistically not the most probable one for representing the magnetic field, in particular at the CMB. However, even if the SH models are by construction currently uncertain, the regional model downward continued to the CMB could represent an attractive constraint to dynamo simulations.

Acknowledgement

This work was funded by the ANR project ANR-13-BS05-0012. The data used in this study are available from the NASA Planetary Data System at http://ppi.pds.nasa.gov.

References

Alexeev, I.I., Belenkaya, E.S., Slavin, J.A., Korth, H., Anderson, B.J., Baker, D.N., Boardsen, S.A., Johnson, C.L., Purucker, M.E., Sarantos, M., Solomon, S.C., 2010. Mercury s magnetospheric magnetic field after the first two messenger flybys. Icarus 209. http://dx.doi.org/10.1016/j.icarus.2010.01.024.
Anderson, B.J., Acuña, M.H., Korth, H., Purucker, M.E., Johnson, C.L., Slavin, J.A., Solomon, S.C., McNutt, R.L., 2008. The structure of Mercury's magnetic field from MESSENGER's first flyby. Science 321, 82–85. http://dx.doi.org/10.1126/science.1159081.
Anderson, B.J., Acuña, M.H., Korth, H., Slavin, J.A., Uno, H., Johnson, C.L., Purucker, M. E., Solomon, S.C., Raines, J.M., Zurbuchen, T.H., Gloeckler, G., McNutt, R.L., 2010. The magnetic field of mercury. Space Sci. Rev. 152. http://dx.doi.org/10.1007/s11214-009-9544-3.
Anderson, B.J., Johnson, C.L., Korth, H., Purucker, M.E., Winslow, R.M., Slavin, J.A., Solomon, S.C., McNutt, R.L., Raines, J.M., Zurbuchen, T.H., 2011. The global magnetic field of mercury from MESSENGER orbital observations. Science 333. http://dx.doi.org/10.1126/science.1211001.
Anderson, B.J., Johnson, C.L., Korth, H., Winslow, R.M., Borovsky, J.E., Purucker, M.E., Slavin, J.A., Solomon, S.C., Zuber, M.T., McNutt Jr., R.L., 2012. Low-degree structure in Mercury's planetary magnetic field. J. Geophys. Res. 117. http://dx.doi.org/10.1029/2012JE004159.
Anderson, B.J., Johnson, C.L., Korth, H., 2013. A magnetic disturbance index for Mercury's magnetic field derived from MESSENGER Magnetometer data. Geochem., Geophys., Geosyst. 14. http://dx.doi.org/10.1002/ggge.20242.
Anderson, B.J., Johnson, C.L., Korth, H., Slavin, J.A., Winslow, R.M., Phillips, R.J., McNutt, R.L., Solomon, S.C., 2014. Steady-state field-aligned currents at Mercury. Geophys. Res. Lett. 41. http://dx.doi.org/10.1002/2014GL061677.
Backus, G., Parker, R., Constable, C., 1996. Foundations of Geomagnetism. Cambridge University Press, Cambridge, UK.
Baerenzung, J., Holschneider, M., Lesur, V., 2014. Bayesian inversion for the filtered flow at the Earth's core-mantle boundary. J. Geophys. Res. 119. http://dx.doi.org/10.1002/2013JB010358.
Cao, H., Aurnou, J.M., Wicht, J., Dietrich, W., Soderlund, K.M., Russell, C.T., 2014. A dynamo explanation for Mercury's anomalous magnetic field. Geophys. Res. Lett. 41. http://dx.doi.org/10.1002/2014GL060196.
Christensen, U.R., 2006. A deep dynamo generating Mercury's magnetic field. Nature 444. http://dx.doi.org/10.1038/nature05342.
Connerney, J.E.P., Ness, NF., 1999. Mercurys Magnetic Field and Interior. Univ. of Arizona Press, Tucson. 24: 494–513.
De Santis, A., Torta, J.M., Lowes, F.J., 1999. Spherical cap harmonics revis- ited and their relationship to ordinary spherical harmonics. Phys. Chem. Earth 24, 935–941.
Finlay, C.C., Lesur, V., Thébault, E., Vervelidou, F., Morschhauser, A., Shore, R., 2016. Challenges handling magnetospheric and ionospheric signals in internal geomagnetic field modelling. Space Sci. Rev. http://dx.doi.org/10.1007/s11214-016-0285-9.
Hauck, S.A., Margot, J.-L., Solomon, S.C., Phillips, R.J., Johnson, C.L., Lemoine, F.G., Mazarico, E., McCoy, T.J., Padovan, S., Peale, S.J., Perry, M.E., Smith, D.E., Zuber, M.T., 2013. The curious case of Mercury's internal structure. J. Geophys. Res. 118. http://dx.doi.org/10.1002/jgre.20091.
Hood, L.L., 2015a. Initial mapping of Mercury's crustal magnetic field: Relationship to the Caloris impact basin. Geophys. Res. Lett. 42. http://dx.doi.org/10.1002/2015GL066451.
Hood, L.L., 2015b. Initial mapping of Mercury's crustal magnetic field: Relationship to the Caloris impact basin. Geophys. Res. Lett. 42. http://dx.doi.org/10.1002/2015GL066451.
Huber, Peter J., 1981. Robust Statistics. Wiley.
Janhunen, P., Kallio, E., 2004. Surface conductivity of Mercury provides current closure and may affect magnetospheric symmetry. Ann. Geophys. 22, 1829–1837. http://dx.doi.org/10.5194/angeo-22-1829-2004.
Johnson, C.L., Purucker, M.E., Korth, H., Anderson, B.J., Winslow, R.M., Al Asad, M.M. H., Slavin, J.A., Alexeev, I.I., Phillips, R.J., Zuber, M.T., Solomon, S.C., Solomon, S.C.,

2012. MESSENGER observations of Mercury's magnetic field structure. J. Geophys. Res. 117. http://dx.doi.org/10.1029/2012JE004217.
Johnson, C.L., Phillips, R.J., Purucker, M.E., Anderson, B.J., Byrne, P.K., Denevi, B.W., Feinberg, J.M., Hauck, S.A., Head, J.W., Korth, H., James, P.B., Mazarico, E., Neumann, G.A., Philpott, L.C., Siegler, M.A., Tsyganenko, N.A., Solomon, S.C., 2015. Low-altitude magnetic field measurements by MESSENGER reveal Mercury ancient crustal field. Science 348, 892–895. http://dx.doi.org/10.1126/science.aaa8720.
Korth, H., Anderson, B.J., Gershman, D.J., Raines, J.M., Slavin, J.A., Zurbuchen, T.H., Solomon, S.C., McNutt, R.L., 2014. Plasma distribution in Mercury's magnetosphere derived from MESSENGER Magnetometer and Fast Imaging Plasma Spectrometer observations. J. Geophys. Res. 119. http://dx.doi.org/10.1002/2013JA019567.
Langlais, B., Lesur, V., Purucker, M.E., Connerney, J.E.P., Mandea, M., 2010. Crustal magnetic fields of terrestrial planets. Space Sci. Rev. 152. http://dx.doi.org/10.1007/s11214-009-9557-y.
Langlais, B., Larnier, H., Amit, H., Thébault, E., Mocquet, A., 2014. A new model for the (geo)magnetic power spectrum, with application to planetary dynamo radii. Earth Planet. Sci. Lett. 401.
Laundal, K.M., Richmond, A.D., 2016. Magnetic coordinate systems. Space Sci. Rev. http://dx.doi.org/10.1007/s11214-016-0275-y.
Lowes, F.J., 1966. Mean square values on the sphere of spherical harmonic vector fields. J. Geophys. Res. 71, 2179.
Lowes, F.J., 1994. The geomagnetic eccentric dipole: facts and fallacies. Geophys. J. Int. 118, 671–679. http://dx.doi.org/10.1111/j.1365-246X.1994.tb03992.x.
Maus, S., 2008. The geomagnetic power spectrum. Geophys. J. Int. 174. http://dx.doi.org/10.1111/j.1365-246X.2008.03820.x.
Ness, N.F., Behannon, K.W., Lepping, R.P., Whang, Y.C., Schatten, K.H., 1974. Observations at Mercury encounter by the plasma science experiment on Mariner 10. Science 185, 159–170.
Ness, N.F., Behannon, K.W., Lepping, R.P., Whang, Y.C., 1975. The magnetic field of Mercury. I. J. Geophys. Res. 80, 2708–2716.
Ng, King H., Beard, David B., 1979. Possible displacement of mercury's dipole. J. Geophys. Res. 84, 2115–2117. http://dx.doi.org/10.1029/JA084iA05p02115.
Oliveira, J.S., Langlais, B., Pais, M.A., Amit, H., 2015. A modified Equivalent Source Dipole method to model partially distributed magnetic field measurements, with application to Mercury. J. Geophys. Res. 120. http://dx.doi.org/10.1002/2014JE004734.
Olsen, N., Glassmeier, K.-H., Jia, X., 2010. Separation of the magnetic field into external and internal parts. Space Sci. Rev. 152, 135–157.
Padovan, S., Wieczorek, M.A., Margot, J.-L., Tosi, N., Solomon, S.C., 2015. Thickness of the crust of Mercury from geoid-to-topography ratios. Geophys. Res. Lett. 42. http://dx.doi.org/10.1002/2014GL062487.
Rivoldini, A., Van Hoolst, T., 2013. The interior structure of Mercury constrained by the low-degree gravity field and the rotation of Mercury. Earth Planet. Sci. Lett. 377. http://dx.doi.org/10.1016/j.epsl.2013.07.021.
Robin, L., 1959. Fonctions Sphériques de Legendre et Fonctions Sphéroidales, vol. I. III. Gauthier-Villars, Paris, France.
Slavin, J.A., Owen, J.C.J., Connerney, J.E.P., Christon, S.P., 1997. Mariner 10 observations of field-aligned currents at Mercury. Planet. Space Sci. 45, 133–141. http://dx.doi.org/10.1016/S0032-0633(96)00104-3.
Slavin, J.A., Krimigis, S.M., Acuña, M.H., Anderson, B.J., Baker, D.N., Koehn, P.L., Korth, H., Livi, S., Mauk, B.H., Solomon, S.C., Zurbuchen, T.H., 2007. MESSENGER: exploring Mercury's magnetosphere. Space Sci. Rev. 131. http://dx.doi.org/10.1007/s11214-007-9154-x.
Thébault, E., 2008. A proposal for regional modelling at the Earth's surface, R-SCHA2D. Geophys. J. Int. 174. http://dx.doi.org/10.1111/j.1365-246X.2008.03823.x.
Thébault, E., Vervelidou, F., 2015. A statistical spatial power spectrum of the Earth's lithospheric magnetic field. Geophys. J. Int. 201. http://dx.doi.org/10.1093/gji/ggu463.
Thébault, E., Schott, J.J., Mandea, M., 2006. Revised spherical cap harmonic analysis (R-SCHA): validation and properties. J. Geophys. Res. 111. http://dx.doi.org/10.1029/2005JB003836.
Thébault, E., Purucker, M., Whaler, K.A., Langlais, B., Sabaka, T.J., 2010. The magnetic field of the Earth's lithosphere. Space Sci. Rev. 155. http://dx.doi.org/10.1007/s11214-010-9667-6.
Thébault, E., Finlay, C.C., Beggan, C., Alken, P., Aubert, J., Barrois, O., Bertrand, F., Bondar, T., Boness, A., Brocco, L., Canet, E., Chambodut, A., Chulliat, A., Coïsson, P., Civet, F., Du, A., Fournier, A., Fratter, I., Gillet, N., Hamilton, B., Hamoudi, M., Hulot, G., Jager, T., Korte, M., Kuang, W., Lalanne, X., Langlais, B., Léger, J.-M., Lesur, V., Lowes, F.J., Macmillan, S., Mandea, M., Manoj, C., Maus, S., Olsen, N., Petrov, V., Ridley, V., Rother, M., Sabaka, T.J., Saturnino, D., Schachtschneider, R., Sirol, O., Tangborn, A., Thomson, A., Tffner-Clausen, L., Vigneron, P., Wardinski, I., Zvereva, T., 2015. International geomagnetic reference field: the twelfth generation. Earth Planets Space 67. http://dx.doi.org/10.1186/s40623-015-0228-9.
Thébault, E., Finlay, C.C., Alken, P., Beggan, C., Canet, E., Chulliat, A., Langlais, B., Lesur, V., Lowes, F.J., Manoj, C., Rother, M., Schachtschneider, R., 2015. Evaluation of candidate geomagnetic field models for IGRF-12. Earth Planets Space 67. http://dx.doi.org/10.1186/s40623-015-0273-4.
Uno, H., Johnson, C.L., Anderson, B.J., Korth, H., Solomon, S.C., 2009. Modeling Mercury's internal magnetic field with smooth inversions. Earth Planet. Sci. Lett. 285, 328–339. http://dx.doi.org/10.1016/j.epsl.2009.02.032.
Verhoeven, O., Tarits, P., Vacher, P., Rivoldini, A., Van Hoolst, T., 2009. Composition and formation of Mercury: Constraints from future electrical conductivity measurements. Plan. Space Sci. 57. http://dx.doi.org/10.1016/j.pss.2008.11.01.
Vervelidou, F., Thébault, E., 2015. Global maps of the magnetic thickness and magnetization of the earth's lithosphere. Earth Planets Space 67. http://dx.doi.org/10.1186/s40623-015-0329-5.
Wicht, J., Heyner, D., 2014. Mercury's Magnetic Field in the MESSENGER Era, pages 223-262. CRC Press, Taylor and Francis Group, Boca Raton, Fl, USA..
Wicht, J., Mandea, M., Takahashi, F., Christensen, U.R., Matsushima, M., Langlais, B., 2007. The origin of Mercury's internal magnetic field. Space Sci. Rev. 132. http://dx.doi.org/10.1007/s11214-007-9280-5.
Winslow, R.M., Anderson, B.J., Johnson, C.L., Slavin, J.A., Korth, H., Purucker, M.E., Baker, D.N., Solomon, S.C., 2013. Mercury's magnetopause and bow shock from MESSENGER Magnetometer observations. J. Geophys. Res. 118. http://dx.doi.org/10.1002/jgra.50237.
Zhong, J., Wan, W.X., Wei, Y., Slavin, J.A., Raines, J.M., Rong, Z.J., Chai, L.H., Han, X.H., 2015. Compressibility of Mercury's dayside magnetosphere. Geophys. Res. Lett. 42. http://dx.doi.org/10.1002/2015GL067063.